Nonlinear Standing Waves of Third Sound in He-II Films

M. T. Reeves[1]

[1]*Department of Mathematics and Physics, University of Queensland, Brisbane Australia*
(Dated: March 6, 2024)

Motivated by recent experiments in superfluid optomechanics, the problem of nonlinear standing waves on a thin film of superfluid helium-4 (He-II) is considered analytically and numerically. Adopting techniques developed for gravity (water) waves, the nonlinear solutions are explored as a function of the wave amplitude and the ratio of the film depth to the wavelength of the excitations. Approximate solutions based on the Stokes expansion are tested against numerical solutions of the full hydrodynamic equations, and the regime of validity of the approximation is outlined. A critical value of depth is found at which the liquid changes behaviour, with shallow layers behaving as a hard spring, and deeper layers as a soft spring. Numerical solutions are also presented for large aspect ratios and moderate amplitudes, where the Stokes expansion breaks down and the standing waves develop into cnoidal or solitary-wave-like solutions. The prediction of hardening for shallow layers is inconsistent with recent experimental observations on third sound waves. Potential resolutions to this discrepancy are discussed.

I. INTRODUCTION

Superfluid helium-4, also known as He-II, has seen an increased interest in recent years in the area of cavity optomechanics [1–7]. Cavity optomechanics focuses on the interaction between confined light and a mechanical degree of freedom, and enables a rich interplay between these electromagnetic and mechanical phenomena. This can give rise to a variety of phenomena which in can provide both a means for controlling and sensing electromagnetic fields and mechanical oscillators alike.

Typically the mechanical component in an optomechanical apparatus is a solid object [8], or in some cases a gas of ultracold atoms [9]. However, helium, which remains a liquid at cryogentic temperatures, and becomes a superfluid below the lambda transition $T_\lambda = 2.17$K, has become an appealing candidate as the mechanical vibration component. This is due to several remarkable properties it possesses, including low refractive index, and zero viscosity []. Being a liquid, superfluid helium is considerably more compliant than the typical solid resonators, which opens the possibility of large (highly nonlinear) oscillations to be excited within the mechanical component.

Some studies have considered acoustic oscillations in bulk He-II [], while others have considered third sound waves, which will be the focus of the present work. Third sound waves are surface excitations on a thin ($\sim$ 1 – 10 nm) film of the superfluid [10]; they similar to gravity waves (such as those occuring on the surface of water) except that the restoring force due to the nonlinear van der Waals attraction between the superfluid and the substrate on which it resides, (rather than gravity). Owing to the extremely thin nature of the helium film and high compliance, extreme nonlinearities can be achieved even with only several photons exciting the film []. The films are also self assembling and adopt the geometry of the resonator [see Fig. 1], facilitating strong coupling between optical and mechanical modes [].These properties are thus highly desirable for quantum operations [5]; it

has been suggested that extremely nonlinear mechanical resonators may offer a route to realizing a mechanical qubit [6].

Optomechanical systems also typically have very high displacement sensitivity [11, 12], and thus provide a novel means to probe the nonlinear hydrodynamics of superfluid helium films. These films provide an intriguing system for fundamental studies of fluid dynamics, as they can access regimes that would otherwise not be possible; the film thicknesses range between $h \sim 10 - 100$nm, the horizontal confinement scales can range from $L \sim 0.1\mu$m – 1cm, the aspect ratio of these systems L/h can thus vary over an enormous range from $\sim$ 1– 10^6 [6, 13]. There are no other real systems which come close to this degree of shallowness without significant attenuation [13]. Experimental measurements also suggest extreme wave amplitudes are possible, wherein the crest-to-trough depth $2a$ is comparable to the liquid depth h such that $2a/h \sim 1$; this regime of extreme aspect ratio and extreme amplitude poses a theoretical challenge, as the associated Ursell number, which is a measure of nonlinearity for surface waves, can be on the order of Ur $= (ka)/(kh)^3 \sim 10^{10}$. The regime of strongly nonlinear dispersive waves goes beyond the standard approaches such as the Korteweg de Vries equation [14, 15], is still not yet well developed theoretically [16]. Additionally, despite considerable theoretical efforts on solitons some 30-40 years ago [14, 15], a definitive and systematic experimental demonstration of such solitons still appears to be lacking. The sensitivity of modern optomechanical experiments, as well as modern fabrication techniques allowing for low-defect substrates, have already provided demonstrations of novel physics in thin-film helium, such as real-time tracking of vortex dynamics [17]. The prospect of observing solitons of third sound in these setups thus also appears promising.

The aim of the present work is to develop theory relevant to nonlinear oscillations which have been observed in helium films. Several experiments have reported characteristics of a nonlinear Duffing oscillator under strong
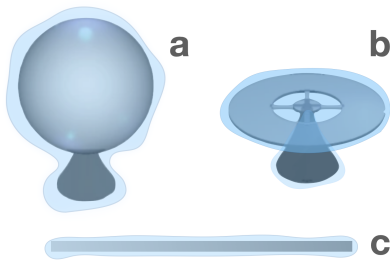
FIG. 1. Example optimechanical microresonators that have been coated in a thin helium film. a: microsphere, b: micro-toroid: c: needle.

FIG. 2. We investigate the standing waves in a 1D hard walled box with ambient liquid depth h, under the influence of a nonlinear van der Waals restoring force.

driving, including, a resonant frequency shift that scales as the square of the response amplitude [13, 18], and the signature 'shark-fin' frequency response at larger driving amplitudes [19]. A surprising feature of all these experiments however is that the nonlinear frequency response ω is a softened one with, $\omega < \omega_0$, where ω_0 is the expected frequency for linear oscillations (i.e. small amplitudes). The observation of softening is surprising because it occurs despite the fact that the liquid layer is extremely shallow; this the opposite behaviour to that of gravity waves in water [20], where in thin fluid layers (aspect ratios $L/h \gtrsim 3$) the liquid behaves as a hard spring rather than a soft one. Baierlein and Ellis [18] argued that the softening observed in their experiment was due to the annular shape of their resonator; it was argued that the central hole significantly modified the mode structure. However more recent experiments conducted on a microdisk [19] exhibit the same softening behaviour despite this geometric feature being absent. Furthermore the behaviour of softening for deep layers and hardening for shallow layers appears to be a quite generic feature for gravity waves, insensitive to the precise geometry and dimensionality of the container [21–25]. This suggests geometry might not be the true reason for this observation, and thus motivates a deeper study into the nonlinear behaviour of nonlinear standing waves of third sound.

Motivated by these recent experiment results, in this paper we consider the problem of two-dimensional nonlinear sloshing of third sound waves. The system is modelled as an ideal liquid of finite depth, with a nonlinear van der Waals restoring force in a 2D box, see Fig. 2. The system can be considered a simple model of a 1D superfluid optomechanical resonator, such as the 'needle' shaped resonator displayed in Fig. 1.

We first investigate the frequency response for arbitrary film thicknesses. This allows perturbative results to be obtained from which insight about the role of the VdW nonlinearities can be obtained. We then focus numerically on a more realistic film scenario, which goes beyond the perturbative approach. In this regime, we identify regimes of cnoidal waves and solitary waves in the standing wave solutions, and the solitary wave solutions are compared against a KdV description.
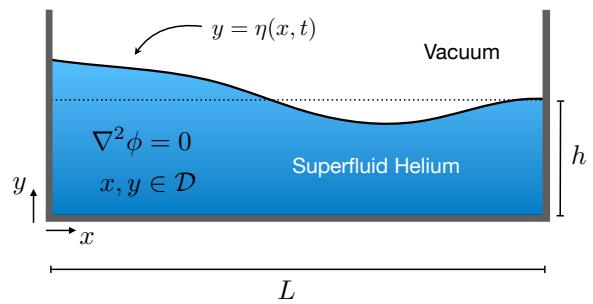
II. MODEL

We will focus on the simplest case of two-dimensional sloshing within a rectangular container, see Fig. 2. This can be considered a simple model of an optomechanical resonator such as the needle-shaped device as per Fig. 1. While in the experimental context the system is naturally driven, the free evolution problem gives insight through calculation of the resonant frequencies under nonlinear dynamics. As the motivating experiments are typically in the milli-Kelvin range [], where the ambient superfluid fraction is near 100%. We may therefore neglect the influence of the viscous normal fluid component, and also the compressibility of the superfluid component [14]. The flow can then be modelled as potential and incompressible flow within the domain, i.e.,

$$\nabla^2 \phi = 0 \quad \text{in} \quad \mathcal{D} \tag{1}$$
$$\mathcal{D} = \{x, y \mid 0 \le x \le L; -h \le y \le \eta(x,t)\}, \tag{2}$$

see Fig. 2. The equations of motion on the surface of the fluid, defined by $y = \eta(x,t)$, are then given by the Euler equations [14, 15]

$$\eta_t + \phi_x \eta_x = \phi_y, \tag{3}$$

$$\phi_t - \alpha \left[\frac{1}{(h+\eta)^3} - \frac{1}{h^3} \right] + \frac{1}{2}(\phi_x^2 + \phi_y^2) = 0. \tag{4}$$

Here α is the van der Waals (vdW) coefficient, h is the mean film thickness, ρ is the fluid density, and $u \equiv \phi_x$ and $v \equiv \phi_y$ are the velocities along x and y respectively [$\mathbf{u} = (u,v)$]. For brevity we have used notation where subscripts denote the derivatives. In Eq.(4) we have also assumed the wavelengths involved are long enough that we may neglect surface tension, although we will return to this point later. We will assume the potential ϕ and the film surface height η must satisfy the spatial boundary conditions

$$\partial_x \phi = 0 \qquad (x = 0, L), \tag{5}$$
$$\partial_y \phi = 0 \qquad (y = -h), \tag{6}$$
$$\partial_x \eta = 0 \qquad (x = 0, L). \tag{7}$$

The first two equations state that the fluid cannot flow through the boundary, while the third imposes a free boundary condition on the surface at the edge of the container.

For small amplitude waves, vdW nonlinearity can be expanded as [6, 18]

$$f(\eta) = -\alpha \left[\frac{1}{(h+\eta)^3} - \frac{1}{h^3} \right] \approx g\eta - g_2 \frac{\eta^2}{h} + g_3 \frac{\eta^3}{h^2} \quad (8)$$

where

$$g = \frac{3\alpha}{h^4}, \qquad g_2 = \frac{6\alpha}{h^4}, \qquad g_3 = \frac{10\alpha}{h^4}. \quad (9)$$

The constant g behaves as an effective gravitational acceleration, and for sufficiently thick films and small surface displacements, the other terms may be neglected and the third sound waves become equivalent to ordinary gravity waves, being sinusoidal surface disturbances with dispersion relation

$$\omega_0^2 = gk \tanh(kh). \quad (10)$$

which, for $kh \ll 1$ reduces to the linear relation $\omega_0 \simeq c_3 k$, where

$$c_3 = (gh)^{1/2}. \quad (11)$$

is the speed of third sound.

A. Conserved quantities

Several conserved quantities for the system provide a useful benchmark for numerical simulations. Firstly, the system may be cast in Hamiltonian form [26, 27]. Defining $\psi(x,t) \equiv \phi(x, \eta(x,t), t)$, the equations may be written as

$$\frac{\partial \eta}{\partial t} = -\frac{\delta H}{\delta \psi} \qquad \frac{\partial \psi}{\partial t} = \frac{\delta H}{\delta \eta}, \quad (12)$$

where the Hamiltonian is

$$H = \int \mathrm{d}x \, [T(x) + V(x)], \quad (13)$$

with

$$T(x) = \frac{1}{2} \int_{-h}^{\eta} |\nabla \phi|^2 \mathrm{d}y, \quad (14)$$

and

$$V(x) = \frac{\alpha}{2} \left[\frac{1}{(h+\eta)^2} - \frac{1}{h^2} \right], \quad (15)$$

being the kinetic and potential energies of the surface waves respectively. In addition to the total energy H, other useful conserved quantities include the mean surface height

$$\bar{\eta} = \int_0^L \eta(x,t) \, \mathrm{d}x = 0, \quad (16)$$

which must be zero to maintain mass conservation by virtue of incompressibility. Similarly the average volume flux across the surface is zero

$$Q = \int (\mathbf{u} \cdot \hat{\mathbf{n}}) \mathrm{d}s = 0, \quad (17)$$

where $\hat{\mathbf{n}}$ is the unit normal to the fluid surface and ds is the line element along the surface $y = \eta(x,t)$.

III. STOKES EXPANSION

A. Procedure Outline

In this section we apply a perturbative approach to calculate the nonlinear frequency correction for third sound waves. The calculation follows closely the method applied by Tadjbakhsh and Keller [20], (hereafter referred to as T&K) who applied the technique to the problem of water waves. Following their approach, we note that the Dirichlet problem can be considered equivalent to the periodic one with waves of wavelength $\lambda = 2L$. Thus, let λ denote the wavelength, $k = 2\pi/\lambda$ the wavenumber, and g denote the acceleration of the effective gravity as per Eq. (9). It is then convenient to convert to dimensionless variables as $\{x, y, h\} \to k^{-1}\{x, y, h\}$, $\omega \to (kg)^{1/2}\omega$, $t \to (kg)^{-1/2}\omega^{-1}t$, for length, frequency, and time respectively. In addition, let a be a measure of the wave height and define

$$\epsilon = ka. \quad (18)$$

The parameter ϵ known as the *wave steepness*, and plays the role of the perturbation parameter for the expansion. Finally, define the dimensionless surface elevation and potential fields as $\eta(x,t) \to \epsilon k^{-1}\eta(x,t)$ and $\phi(x,y,t) \to \epsilon g^{1/2} k^{-3/2} \phi(x,y,t)$.

In the chosen dimensionless units, the equations of motion take the form

$$\omega \eta_t + \epsilon \phi_x \eta_x = \phi_y, \quad (19)$$

$$-\frac{h}{3} \left[\frac{1}{(1+\epsilon \eta/h)^3} - 1 \right] + \epsilon \omega \phi_t + \frac{1}{2}\epsilon^2 (\phi_x^2 + \phi_y^2) = 0 \quad (20)$$

on $y = \epsilon \eta(x,t)$. Eqs. (19) and (20) are our equivalent of T&K's Eqs. (3) and (2), respectively and the remaining equations required to solve the problem are identical to those outlined in Eqs. (1)–(8) of T&K [20]. We expand the solution as a perturbation series in ϵ as

$$\eta(x,t,\epsilon) = \eta^0(x,t) + \epsilon \eta^1(x,t) + \frac{1}{2}\epsilon^2 \eta^2(x,t)$$
$$\phi(x,y,t,\epsilon) = \phi^0(x,y,t) + \epsilon \phi^1(x,y,t) + \frac{1}{2}\epsilon^2 \phi^2(x,y,t)$$
$$\omega(\epsilon) = \omega_0 + \epsilon \omega_1 + \frac{1}{2}\epsilon^2 \omega_2. \quad (21)$$

The only difference to the gravity wave case is that the restoring force is also nonlinear, and so we additionally require an expansion of the VdW potential up to third

order in ϵ:

$$-\tfrac{h}{3}\left[\tfrac{1}{(1+\epsilon\eta/h)^3}-1\right] \approx \epsilon\eta^0 + \epsilon^2\left(\eta^1 - 2\tfrac{(\eta^0)^2}{h}\right)$$
$$+ \epsilon^3\left(\tfrac{10}{3}\tfrac{(\eta^0)^3}{h^2} - \tfrac{4\eta^0\eta^1}{h} + \tfrac{1}{2}\eta^2\right). \quad (22)$$

After substituting Eq. (22) into Eq. (20) the zeroth order solution is found by taking the limit $\epsilon \to 0$ in Eqs. (19) and (20); the solution is the same as in the case of gravity waves on water of finite depth h, viz.:

$$\eta^0 = \sin t \cos x \qquad (23)$$

$$\phi^0 = \frac{\omega_0}{\sinh h}\cos t \cos x \cosh(y+h) \qquad (24)$$

$$\omega_0^2 = \tanh h. \qquad (25)$$

The first order terms can then be found by differentiating Eqs. (19) and (20) with respect to ϵ, then once again taking $\epsilon \to 0$ and inserting the known expressions for the zeroth order solution. Once the first order terms are found, the second order terms can be found by repeating the same procedure. The details of the calculation are lengthy, but are identical to the procedure that is already laid out clearly and in detail in Ref. [20] and we thus will not reiterate them here. Instead we will outline the main findings and discuss the results in comparison with the gravity wave results of Ref. [20].

B. Results

For completeness the full solutions for the expressions in Eq. (21) are provided in Appendix A, although we will not discuss them in full detail here. Of primary interest for our purposes is the resonant frequency ω. The frequency correction for the nonlinear standing waves is found to be

$$\omega = \omega_0 + \tfrac{1}{2}\epsilon^2\omega_2 \qquad (26)$$

(ω_1 is found to be zero), and

$$\omega_2 = \tfrac{1}{32}\left(9\omega_0^{-7} - 12\omega_0^{-3} - 3\omega_0 - 2\omega_0^5\right) \qquad (27)$$

$$- \tfrac{1}{4h}\left(3\omega_0^{-5} + \omega_0^{-1} + 2\omega_0^3\right) \qquad (28)$$

$$+ \tfrac{1}{8h^2}\left(4\omega_0^{-3} + 7\omega_0\right) \qquad (29)$$

where ω_0 is given by Eq. (25). Eqs. (26)–(29) show that to leading order, the frequency response is indeed expected to be of the Duffing type, being equal to a constant times the square of the oscillator (wave) amplitude.

The first frequency correction term, Eq. (27), is identical to the result obtained by T&K for gravity waves, while the other two terms, Eq. (28) and Eq. (29), respectively represent the corrections due to the g_2 and g_3 terms in the expansion of the VdW potential as per Eq. (9). These are exclusively "softening" and "hardening" terms respectively, with Eq. (28) being negative for
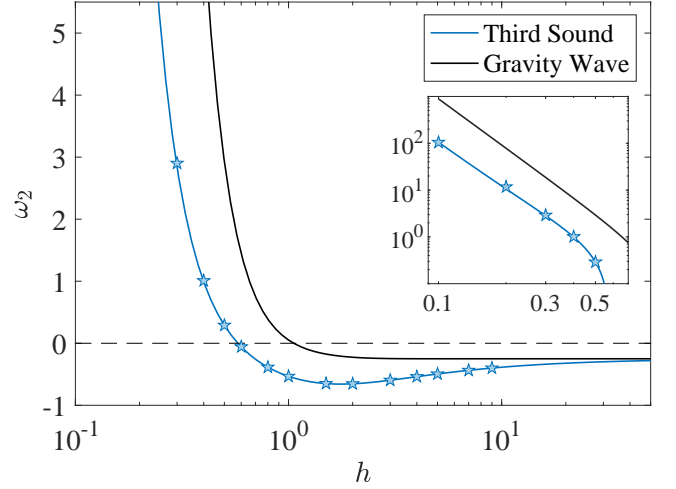

FIG. 3. Comparison of the frequency correction ω_2 vs. liquid depth h for the cases of gravity waves [Eq. (27)] and third sound [Eqs. (27)–(29)]. Star markers show results from numerical simulations which includes the full van der Waals potential [see Sec. IV]. Inset shows the same data (extended to lower h) on a log-log scale in the regime $h < h^*$ where $\omega_2 > 0$.

all h and Eq. (29) being positive for all h. The two Van der Waals terms are of comparable magnitude, and both monotonically tend to zero as $h \to \infty$.

Several noteworthy observations can be made from the resulting expression for ω_2, which we plot in Fig. 3, along with the pure gravity wave result, Eq. (27) for comparison. Firstly, ω_2 changes sign at the critical depth

$$h^* = 0.578819\ldots \qquad (30)$$

Depths $h < h^*$ produce hardening ($\omega_2 > 0$), and depths $h > h^*$ produce softening ($\omega_2 < 0$). This is the same behaviour as in water waves, however here h^* is roughly half the result for water waves, $h_g^* = 1.05809\ldots$ This gives a critical tank length-to-depth ratio of approximately $L/h \sim 5.5$ for third sound, compared to the ratio of approximately $L/h \sim 3$ for water waves. Secondly, there exists a finite value of h

$$h_{\min} = 1.75386\ldots, \qquad (31)$$

where ω_2 is minimized. No such value exists in the case of water waves, where the frequency is a monotonically decreasing function of h. This value of h corresponds to an aspect ratio of $L/h \sim 1.8$. Thirdly, in the limit $h \to \infty$ we recover Rayleigh's original result for deep water waves, $\omega_2 \to 1/4$. The limit is approached slowly, however, with the asymptotic behaviour

$$\omega_2 \simeq -\tfrac{1}{4} - \tfrac{3}{2}h^{-1} + \tfrac{11}{8}h^{-2}, \qquad h \gg 1. \qquad (32)$$

This result may have limited relevance, in since very thick films ($h \gtrsim 100$ nm) third sound waves become difficult to distinguish from gravity waves on bulk superfluid helium. We have also not included the influence of physical

gravity, which would renormalize the effective value of g for thick films. We note however that third sound experiments have been conducted on films up to several μm in thickness have been conducted in microgravity [28]. The regime could also be accessed by decreasing the confinement scale L, however this would increase the contributions of surface tension, which we have ignored in the present treatment.

In the shallow liquid limit is more relevant to realistic He-II films, and this is the regime where surface tension can be more realistically neglected. In this regime, the frequency is predicted to diverge as

$$\omega_2 \sim \tfrac{1}{32} h^{-7/2} \quad \text{as} \quad h \to 0, \tag{33}$$

giving the relative frequency shift

$$\frac{\omega - \omega_0}{\omega_0} \equiv \frac{\Delta\omega}{\omega_0} \sim \frac{1}{64}\left(\frac{\epsilon}{h^2}\right)^2 \tag{34}$$

The scaling is the same as the water wave case, but the prefactor is reduced by a factor of 9 [see Fig. 3, inset]. Interestingly, inspecting the three terms in Eqs. (27)–(29), we find that the hardening contributions from the hydrodynamic nonlinearity [Eq. (27)] and the cubic van der Waals nonlinearity [Eq. (29)] are individually both weaker than the softening term from the quadratic van der Waals nonlinearity [Eq. (28)]; it is only combined that both hardening terms together are strong enough to overcome the softening term and overall give rise to a hardening effect for small liquid depths h. This finding is consistent with the arguments put forward in Ref. [18], which argued that including only the g_2 term would give incorrect results. In the approach employed here, both terms are naturally accounted for when the perturbation series machinery is correctly applied to the nonlinear restoring potential expansion, [Eq. (22)].

C. Validity

An important consideration is the ratio of successive terms in the expansion, as the perturbation expansion is only valid when the correction term remains small. The validity can be assessed by inspecting the maximum surface profile deviation, $H = \max[|\eta(x,t)|]$. Consulting our results for η in the Appendix, H can be written as:

$$H = \epsilon + \tfrac{1}{2}\epsilon^3(b_{11} + b_{13} - b_{31} - b_{33}) \tag{35}$$

where the values b_{ij} relate to the Fourier coefficients of the solution for η^2 and are given in Appendix A. For $h \ll 1$ the above expression simplifies to

$$H \simeq \epsilon\left(1 + \tfrac{3}{256}\epsilon^2 h^{-6}\right). \tag{36}$$

Restoring units, the second term being small amounts to

$$\text{Ur} \equiv \frac{ka}{(kh)^3} \ll \frac{16}{\sqrt{3}} \sim 9, \tag{37}$$

where Ur is the Ursell number. A similar validity requirement can be obtained from the potential, as convergence of the series expansion requires the ratio

$$\left|\frac{\epsilon^2\phi^1}{\epsilon\phi^0}\right| = \frac{1}{16}\frac{\epsilon}{h^3} \ll 1, \tag{38}$$

implying Ur $\ll$ 16. These constraints are less stringent than the corresponding constraints on gravity waves, which are smaller by approximately a factor of three; it appears the nonlinear effects in third sound increase more gradually than for water waves, due to the partial cancellation between hardening and softening effects. Finally, notice that these constraints are more strict than what one would deduce from the frequency correction, from which one would incorrectly deduce the constraint $\epsilon/h^2 \ll 1$.

IV. NUMERICAL STANDING WAVE SOLUTIONS

We compliment the analytical approach of the previous section with a numerical study of the standing wave solutions, where we may include the full effects of the hydrodynamic nonlinearity and the van der Waals nonlinearity. To numerically solve the equations for the standing waves solutions, we use the semi-Lagrangian boundary integral approach developed by Roberts [29]. This approach has been used by Smith and Roberts [30] to study nonlinear standing wave solutions for water waves, and our procedure is very similar to theirs. In brief, the method finds nonlinear standing wave solutions via a shooting-type method; the procedure involves starting with a guess solution for the surface profile, which is stationary at $t = 0$, and integrating the equations of motion for a trial period
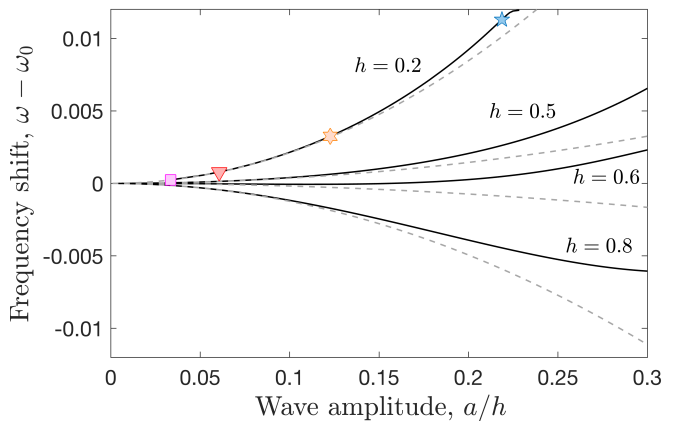

FIG. 4. Frequency shifts ω_2, obtained by solving the full nonlinear standing wave problem numerically, for several different film thicknesses h (solid lines) near the critical depth h^*. The perturbation theory result (dashed lines), [Eqs. (27)-(29)], for each value of h is shown for comparison. The markers indicated on the curve for $h = 0.2$ correspond to the surface profile examples shown in Fig. 5
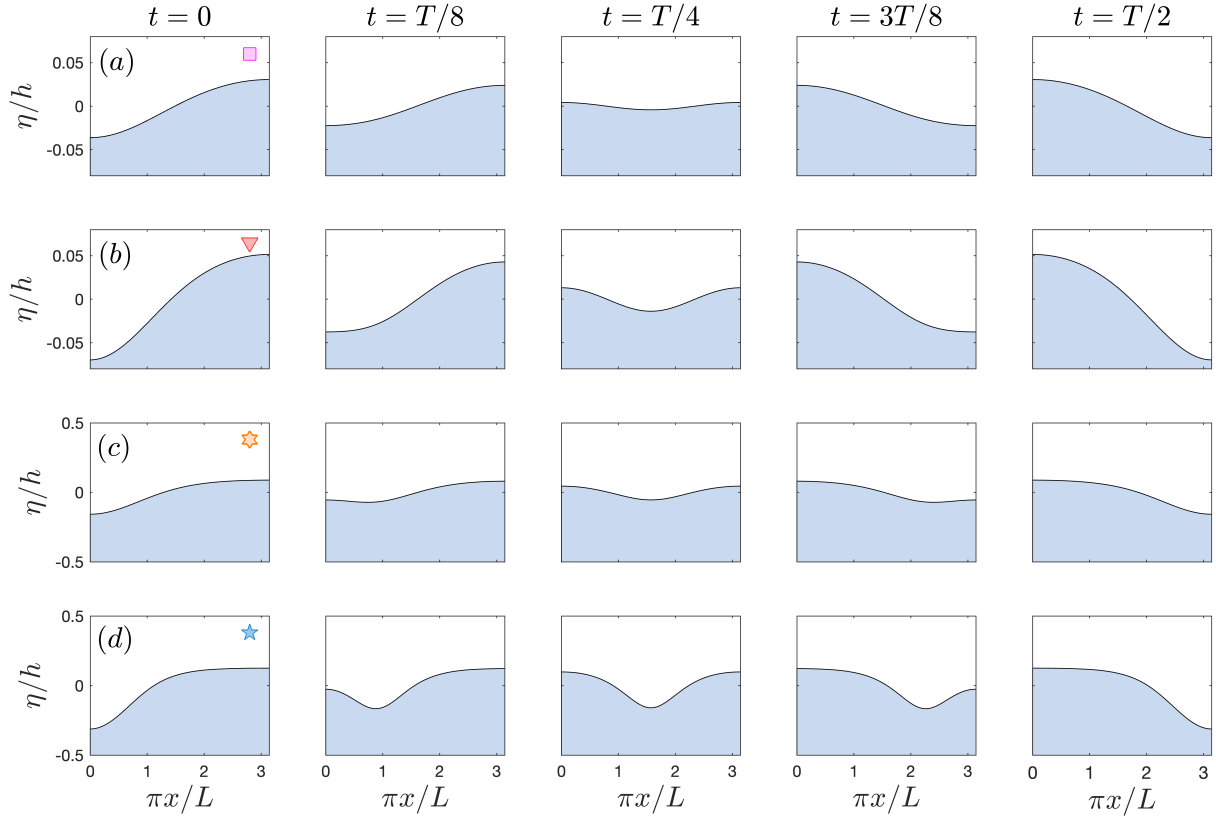
FIG. 5. Example surface profiles $\eta(x,t)$ for $h = 0.2$ and varying wave amplitudes. Colored markers correspond to examples shown shown in Fig. 4 with the same marker type.
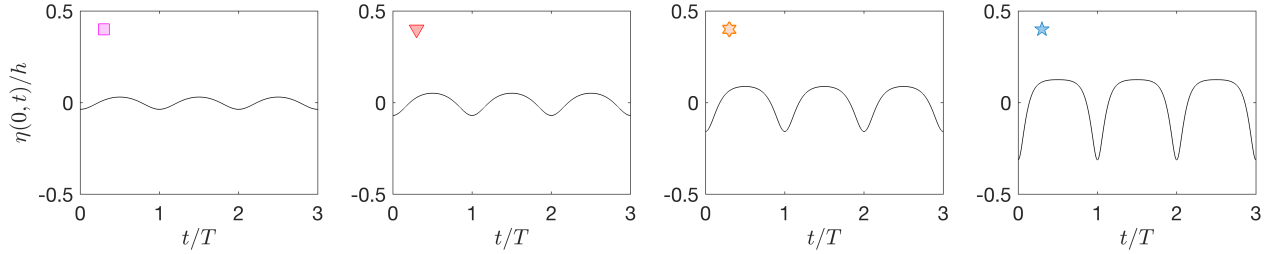

FIG. 6. Example time series of the surface at the left wall $\eta(0,t)$ for $h = 0.2$ and varying wave amplitudes. Colored markers correspond to the examples shown in Fig. 4 and Fig. 5 with the same marker type.

T. The trial surface profile and period are iteratively adjusted using Newton-type methods, until a periodic solution is found within a specified tolerance. The validity of the solutions are verified using the conserved quantities outlined in Sec. II A. For completeness, full details of the calculation are outlined in Appendix B.

A.   Thick Films $(kh \sim 1)$

We first consider thick films. These are not necessarily experimentally realistic, but they nonetheless provide a useful point of comparison against theory. We plot the numerical solutions for the the frequencies against the

wave amplitude

$$a = (\max[\eta] - \min[\eta])/2 \qquad (39)$$

which is equivalent to the wave steepness [Eq. (18)] up to order ϵ^3, cf. Eq. (35). The frequencies are shown for several different values of h in Fig. 4. The general behaviour confirms the perturbation theory predictions of the previous section — for small amplitudes, we find depths $h > h^*$ exhibit softening, whereas depths $h < h^*$ exhibit hardening. The perturbation theory solutions are also potted as dashed lines; for the examples shown, the agreement is generally quite good until the amplitude is approximately 10–15% of the film thickness. Within the vicinity of $h = h^*$, we observe non-monatonic behaviour of the frequency, a behaviour which is not captured by the perturbation series result. For example, the case $h = 0.6 > h^*$ shown exhibits softening at small a but transitions to hardening at larger values of a. This non-monatonic behaviour near the critical depth has also been noted for water waves [21]. We also compare the validity of the perturbation theory description by fitting a value for ω_2, i.e, fitting a relation of the form $\omega - \omega_0 = \frac{1}{2}\omega_2\epsilon^2$ to the small amplitude regions of the full numerical solutions, where the curves are well approximated as quadratic. The values for ω_2 extracted from the fits to the numerical solutions are presented in Fig. 3. It is seen that the values are in good agreement with the analytical result.

Examples of the surface profile vs. time are shown in Fig. 5, for the particular cases highlighted by the markers on the $h = 0.2$ curve in Fig. 4. The height of the surface at the left wall, which is a quantity that can be extracted optomechanically, is also shown for these examples in Fig. **??**. The smaller amplitude excitations are approximately sinusoidal, whereas the larger amplitudes exhibit a deep tough at one end of the container and a relatively flat profile at the other end of the container.

B. Thinner Films ($kh \ll 1$)

We now turn to thinner films, which go beyond the scope of the perturbation series expansion. We focus on the case $h = 0.025$, which corresponds to an aspect ratio of $L/h \sim 125$. This would correspond, for example, to a resonator length of $1.25\mu m$ for a 10nm thick film; this is comparable to parameters considered by previous optomechanical experiments [6].

The frequency shift $\omega - \omega_0$ for this case is shown in Fig. 7. It can be seen that the system exhibits hardening, inline with the perturbation theory prediction. However, the behaviour quickly deviates from quadratic; instead, the frequency shift is more consistent with a relation of the form $(\omega - \omega_0) \sim a^{1.25}$, suggesting an exponent of 5/4.

Further insight into this behaviour is gained by inspecting the surface profiles, shown for several different wave amplitudes in Fig. 8. At lower amplitudes (a,b), the solutions consist not of a standing wave but instead
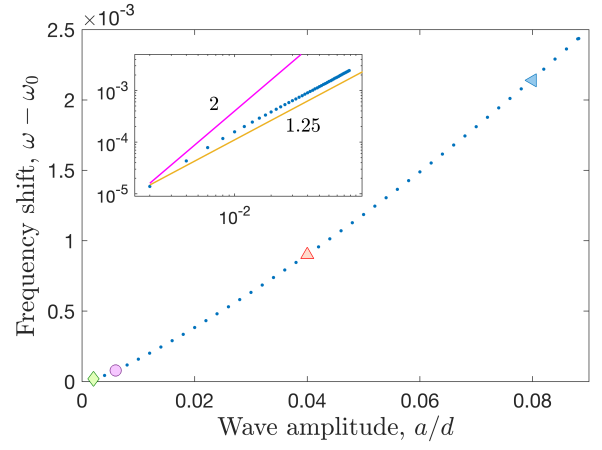

FIG. 7. Observed frequency shift $\omega - \omega_0$, plotted vs. wave amplitude a, for the case $h = 0.025$. Inset shows the same data plotted on a log-log scale. Lines proportional to a^2 and $a^{1.25}$ are shown for comparison.

of a broad surface depression which traverses back and forth between the two walls. In fact, we find the solution is a cnoidal wave, well approximated by the form $A - B\mathrm{cn}(x|k)^2$, where $\mathrm{cn}(x|k)$ is the Jacobi elliptic cosine function of modulus k. Such solutions have been considered in the gravity wave context by Bridges [31], where the lowest order solutions are a linear superposition of leftward and rightward travelling cnoidal waves.

Upon further increase of the wave amplitude (c,d), the travelling waves become increasingly narrow, eventually becoming solitary waves. This suggests further insight can be gained from a KdV description. Nakajimia [14] derived a KdV equation for third sound of the form

$$\frac{\partial \eta}{\partial t} + \frac{g}{2c_3}\left[\eta\frac{\partial \eta}{\partial x} - \frac{1}{3}h^3\frac{\partial^3 \eta}{\partial x^3}\right] = 0 \qquad (40)$$

where $c_3 = \pm(gh)^{1/2}$. The nonlinear term is of the opposite sign of the water wave equation due to the contribution from the softening term $g_2 = -2g$, which makes the soliton solutions trough-like rather than crest-like excitations. Under the following choice of units for length and time

$$\ell = \sqrt[3]{2}\,d \qquad \tau = 12\left(\frac{d}{g}\right)^{1/2} \qquad (41)$$

the equation is expressed in standard form

$$\eta_t + 6\eta\eta_x - \eta_{xxx} = 0. \qquad (42)$$

It therefore admits soliton solutions of the form

$$\eta = A - H\,\mathrm{sech}^2\left(\frac{x - ct}{\Delta}\right), \qquad (43)$$

with

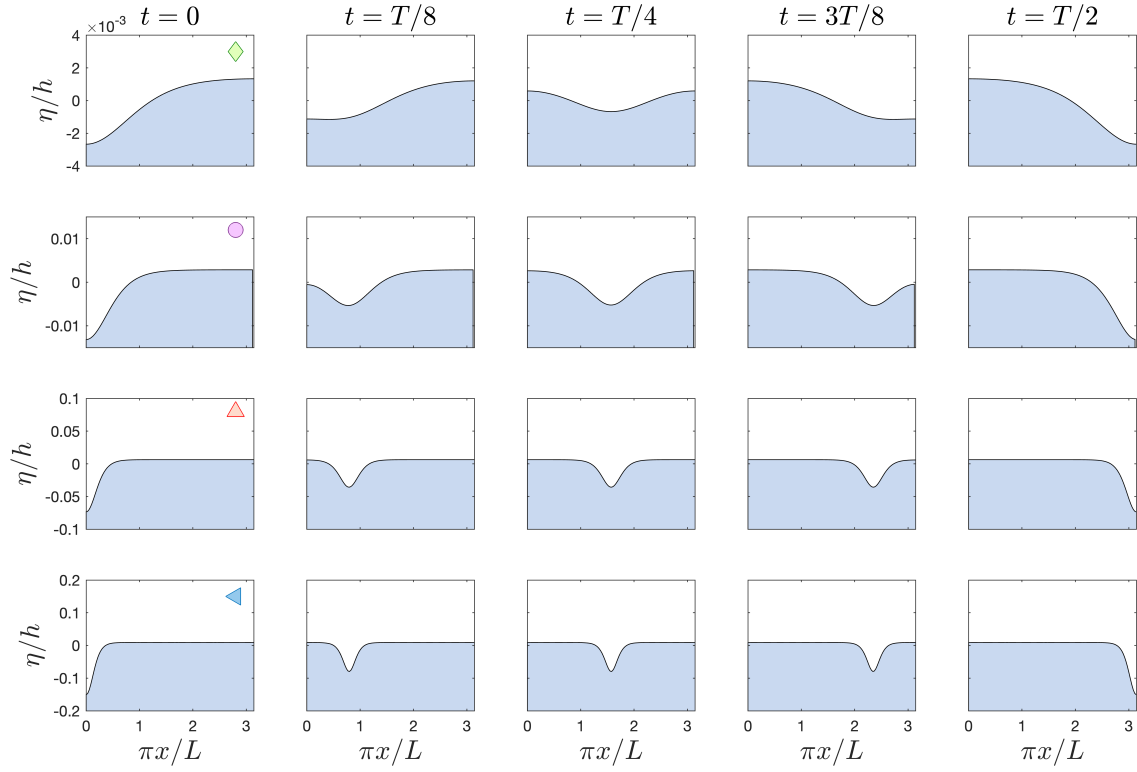$$\Delta = \sqrt{\frac{2h}{H}}\ell, \qquad c = (gh)^{1/2}\left\{1 + \frac{1}{2}\frac{H}{h}\right\}. \qquad (44)$$

FIG. 8. Example surface profiles $\eta(x,t)$ evolving over the half-period, $t \in [0, T/2]$ for $h = 0.025$ and increasing amplitudes. The colored markers
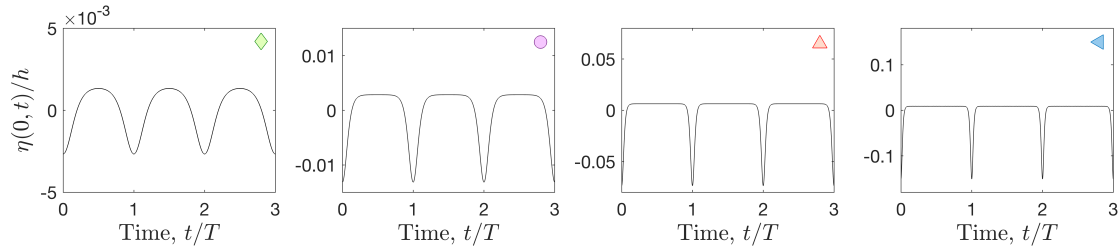

FIG. 9. Surface height at the left wall of the container vs time, $\eta(0,t)$, evolving over multiple periods, $t \in [0, 5T]$ for $h = 0.025$ and increasing amplitudes. The amplitudes are the same as those shown in Fig. 8.

Further, assuming $\Delta \ll L$, the height condition Eq. (16), gives

$$A \simeq \frac{2H\Delta}{L} = \frac{2^{11/6} h \sqrt{Hh}}{L}.$$ (45)

Neglecting corrections due to collisions with the walls, the frequency of a soliton solution will be approximately $\omega = 2\pi/T$, where $T = 2L/c$ is the time round trip time for the soliton. Hence the frequency is

$$\omega = \frac{\pi c}{L} \approx \omega_0 \left(1 + \frac{1}{2}\frac{H}{h} \right).$$ (46)

This expression does not include corrections due to the shift in the film height, which will arise due to the presence of the soliton ($h \rightarrow h + A$). However by Eq. (45) this correction is of the order $\mathcal{O}(\sqrt{Hh}/L) \ll H/h$ and can thus be neglected.

In Fig. 10, we compare the properties numerical solitary waves with the solitons from Nakajimia's KdV equation. To compare with the KdV prediction, we fit the soliton solution Eq. (43) to the numerical solution, to obtain values for H and Δ. We fit using the surface profile at the time $t = T/4$, which is the time when the soliton is in the middle of the container. This choice is necessary to correctly compare with the KdV prediction, which corresponds to a "free" soliton and thus does not account for interactions with the container walls (as can be see in Fig. 8, the solitary wave becomes higher and narrower when it collides with the wall). At $t = T/4$, the solitary wave is in the middle of the container, ensuring it is located as far as possible from the container walls.

Fig. 10(a) compares the value of Δ obtained from fitting Eq. (43) to the numerical profiles vs. the prediction of Eq. (44) from the KdV equation. While the KdV prediction is marginally smaller than the fitted values, the agreement is quite good. We find very good agreement between the fitted values and Eq. (44) if the KdV prediction is scaled by a small percentage, $\Delta \rightarrow 1.07\Delta$. In Fig. 10(b), we plot the frequency shift $(\omega - \omega_0)/\omega_0$, against the free height of the solitary wave H/h. It is clear that the frequency shift is indeed linear in the free soliton amplitude, although the slope is signifantly smaller than the value of $1/2$ as predicted by the KdV equation (a line of best fit gives a slope of ≈ 0.16).

From Fig. 10(b), it is also clear that the scaling of $\omega \sim a^{5/4}$, as shown in Fig. 7, is due to measuring the soliton height at the wall, rather than the height when it is freely propagating through the bulk of the liquid, which is more characteristic of the "true" height. Since the collision of the soliton with the wall is equivalent to colliding with an equal soliton propagating in the opposite direction, a corollary of this result is that we expect equal solitons This would be an important consideration experimentally, in setups where the surface profile readout is located near one of the walls of the container [].
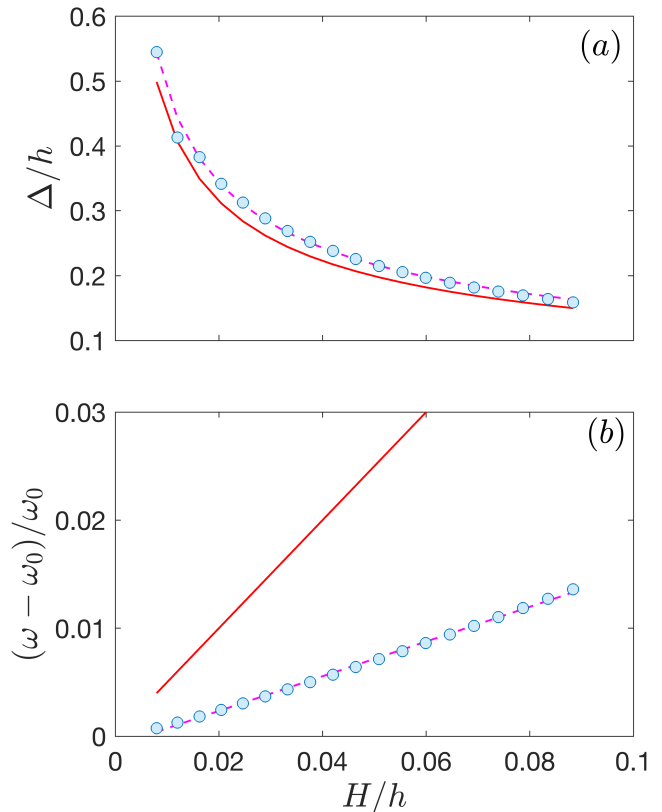

FIG. 10. Comparison between the properties of the soliton-like numerical solutions with those of KdV solitons, Eq. (44). (a) Soliton width Δ at time $t = T/4$. (b) Frequency shift $((\omega - \omega_0)/\omega_0$. Both quantities are plotted against the soliton height $H = \max(\eta(x, T/4)) - \min(\eta(x, T/4))$. Shown for comparison are the expected values for the KdV solitons, Eq. (44) (solid, red), along side lines of best fit (dashed, magenta).

V. DISCUSSION AND OUTLOOK

Our analytical approach based on the Stokes expansion shows good agreement with the full numerical solutions for small Ursell numbers, $\mathrm{Ur} = (ka)/(kh)^3 \lesssim 9$. A shortcoming of the analytical approach used here is that it cannot handle fairly modest amplitudes at extreme aspect ratios, since in this situation the Ursell number quickly becomes too large. Under these conditions, the system is more appropriately described in terms of cnoidal waves or solitions of the KdV equation []. Although this regime is more computationally expensive to investigate, the numerical approach outlined herein is nonetheless capable of probing these limits. We remark that hardening still expected under these theories; the solitary waves increase in speed with amplitude, and hence their frequency increases. Similarly, standing cnoidal waves have been considered in the case of water waves by XXX [], who found that the frequency hardens linearly. Our findings for the stokes expansion outlined here indicate that the van der Waals nonlinearity will not change this behaviour qualitatively for third sound, although we would expect the

hardening prediction to be not as extreme as in the case of water waves. We note that many resonances appear for the shallower films, and the pseudoarclength continuation method outlined by Smith and Roberts [], which can more easily accomodate such resonances, would therefore be more appropriate than the dogleg method used here.

In our opinion, there are two likely culprits that would produce softening in He-II films, despite their extremely shallow aspect ratios. One possible explanation comes from the inclusion of surface tension. The influences of surface tensions was considered in the water wave context by Concus, building on the work of T&K. The inclusion of surface tension was considered perturbatively by Concus [32]. He obtained a similar frequency shift result to that of T&K, viz.

Increasing surface tension for shallow liquids can change the behaviour from softening to hardening. The analysis of Concus can be straightforwardly extended to the third sound case, although the analytical calculations and the resulting expressions are naturally considerably more invovled and complex than those outlined here.

We believe the other likely culprit is the boundary conditions. In the case of damped liquid oscillators, which are liquid oscillators tuned to cancel out vibration frequencies, it has been found that a container which has sloped walls, rather than vertical walls as considered here,

can exhibit softening in regimes where the vertical walled containers exhibit hardening. This is because the liquid can run up the inclined slope of the container during sloshing.

The method used herein can also be readily adapted to an interface between fluids of two different densities, and could thus be used to investigate mixture films of ^{3}He-^{4}He mixture films [33]. The exploration of larger amplitude waves should also be possible within the model, using the pseudoarclength continuation to avoid the complication of resonances [].

VI. CONCLUSION

ACKNOWLEDGEMENTS

Appendix A: Full Perturbation Theory Solution

Following the procedure of T&K [20], the full solution for the third sound waves, to second order in ϵ, is given by

$$\eta(x,t,\epsilon) = \eta^0(x,t) + \epsilon\eta^1(x,t) + \tfrac{1}{2}\epsilon^2\eta^2(x,t) \tag{A1}$$

$$\phi(x,y,t,\epsilon) = \phi^0(x,y,t) + \epsilon\phi^1(x,y,t) + \tfrac{1}{2}\epsilon^2\phi^2\eta^2(x,y,t) \tag{A2}$$

$$\omega(\epsilon) = \omega_0 + \epsilon\omega_1 + \tfrac{1}{2}\epsilon^2\omega_2. \tag{A3}$$

The linear, zeroth order contribution is the familiar solution for ordinary gravity waves

$$\eta^0 = \sin t \cos x, \qquad \phi^0 = \frac{\omega_0}{\sinh h}\cos t \cos x \cosh(y+h), \qquad \omega_0^2 = \tanh h. \tag{A4}$$

The first-order corrections are

$$\omega_1 = 0 \tag{A5}$$

$$\eta^1 = \tfrac{1}{8}\left[(\omega_0^2 + \omega_0^{-2} + \tfrac{4}{h}) + (\omega_0^{-2} - 3\omega_0^{-6} + \tfrac{4}{h}\omega_0^{-4})\cos 2t\right]\cos 2x \tag{A6}$$

$$\phi^1(x,y,t) = \beta_0 + \tfrac{1}{8}(\omega_0 - \omega_0^{-3} + \tfrac{4}{h}\omega_0^{-1})t - \tfrac{1}{16}(3\omega_0 + \tfrac{4}{h}\omega_0^{-1} + \omega_0^{-3})\sin 2t$$
$$- \frac{3}{16\cosh 2h}[\omega_0^{-7}(\omega_0^4 + 1)(\omega_0^4 + \tfrac{4}{3h}\omega_0^2 - 1)]\sin 2t \cos 2x \cosh 2(y+h) \tag{A7}$$

where β_0 is an arbitrary constant. The corrections due to the g_2 van der Waals nonlinearity manifest as the terms with the prefactors of $4/h$ and $4/3h$; discarding these terms one recovers the result of T&K. From the first order correction η^1, it can be seen that, unlike in the linear approximation, the surface does not become flat at any point

during the dynamics. At this level of approximation, it can also already be seen that the excitations for third sound are surface depressions, in contrast to the peaks occurring for gravity waves; for example at $t = 0$, the surface shows a central crest for gravity waves and a trough for third sound. We also note that T&K have a typo in the first term of η^1; in their Eq. (30) the factor reads $(\omega_0^2 - \omega_0^{-2})$ when it should read $(\omega_0^2 + \omega_0^{-2})$. This error does not appear to have affected their later expressions, which are consistent with ours, and which have been verified using Mathematica.

The full second order solution is as follows. The second order frequency is given by

$$\omega_2 = \frac{1}{32} \left(9\omega_0^{-7} - 12\omega_0^{-3} - 3\omega_0 - 2\omega_0^5 \right) - \frac{1}{4h} \left(3\omega_0^{-5} + \omega_0^{-1} + 2\omega_0^3 \right) + \frac{1}{8h^2} \left(4\omega_0^{-3} + 7\omega_0 \right). \tag{A8}$$

The potential is

$$\phi^2(x, y, t) = \sum_{n,m=\{1,3\}} \beta_{m,n} \cos mt \cos nx \cosh n(y + h) \tag{A9}$$

with

$$\beta_{11} = 0 \tag{A10}$$

$$\beta_{31} = \frac{1}{128 \cosh h} \left[\frac{1}{h^2} \left(-\frac{48}{\omega_0^5} - \frac{60}{\omega_0} \right) + \frac{1}{h} \left(\frac{24}{\omega_0^7} - \frac{104}{\omega_0^3} \right) - \frac{31}{\omega_0} + \frac{62}{\omega_0^5} + \frac{9}{\omega_0^9} \right] \tag{A11}$$

$$\beta_{13} = \frac{1}{128 \cosh 3h} \left(3\omega_0^4 + 1 \right) \left[\frac{1}{h^2} \left(\frac{12}{\omega_0} - \frac{16}{\omega_0^5} \right) + \frac{1}{h} \left(16\omega_0 - \frac{24}{\omega_0^3} + \frac{8}{\omega_0^7} \right) + 2\omega_0^3 + \frac{3}{\omega_0^9} - \frac{5}{\omega_0} \right] \tag{A12}$$

$$\beta_{33} = \frac{1}{128 \cosh 3h} \left(3\omega_0^4 + 1 \right) \left[\frac{1}{h^2} \left(-\frac{16}{\omega_0^9} - \frac{20}{3\omega_0^5} \right) + \frac{1}{h} \left(\frac{24}{\omega_0^{11}} - \frac{24}{\omega_0^7} \right) - \frac{13}{\omega_0^5} + \frac{22}{\omega_0^9} - \frac{9}{\omega_0^{13}} \right] \tag{A13}$$

And the surface profile is given by

$$\eta^2(x, t) = \sum_{n,m=\{1,3\}} b_{m,n} \sin mt \cos nx \tag{A14}$$

where

$$b_{11} = \frac{1}{32} \left(\frac{3}{\omega_0^8} + \frac{6}{\omega_0^4} + 2\omega_0^4 - 5 \right) + \frac{1}{4h} \left(\frac{1}{\omega_0^6} - \frac{2}{\omega_0^2} + 2\omega_0^2 \right) - \frac{1}{8h^2} \left(7 + \frac{4}{\omega_0^4} \right) \tag{A15}$$

$$b_{31} = \frac{1}{128} \left(\frac{3}{\omega_0^8} + \frac{18}{\omega_0^4} - 5 \right) + \frac{1}{16h} \left(\frac{1}{\omega_0^6} - \frac{3}{\omega_0^2} \right) - \frac{1}{32h^2} \left(5 + \frac{4}{\omega_0^4} \right) \tag{A16}$$

$$b_{13} = \frac{3}{128} \left(\frac{9}{\omega_0^8} + \frac{27}{\omega_0^4} - 15 + \omega_0^4 + 2\omega_0^8 \right) + \frac{3}{16h} \left(\frac{3}{\omega_0^6} - \frac{4}{\omega_0^2} + 3\omega_0^2 + 2\omega_0^6 \right) + \frac{3}{32h^2} \left(5 - \frac{12}{\omega_0^4} + 3\omega_0^4 \right) \tag{A17}$$

$$b_{33} = \frac{3}{128} \left(1 - \frac{9}{\omega_0^{12}} + \frac{3}{\omega_0^8} - \frac{3}{\omega_0^4} \right) + \frac{1}{16h} \left(\frac{9}{\omega_0^{10}} + \frac{2}{\omega_0^6} + \frac{1}{\omega_0^2} \right) - \frac{1}{96h^2} \left(5 + \frac{36}{\omega_0^8} + \frac{27}{\omega_0^4} \right). \tag{A18}$$

In all the above, the terms involving factors of $1/h$ and $1/h^2$ correspond to the softening and hardening contributions from the nonlinear terms associated with g_2 and g_3 respectively. The other terms are identical to those given by T&K.

Appendix B: Numerical Method

The essence of the formulation is to model the fluid interface as a vortex sheet, which may be modelling as a set of singularities (point vortices) along the surface. The strengths (circulations) of the singularities depend on the instantaneous distribution of the surface profile. The interface $\eta(x, t)$ is parameterized using an auxilliary variable j,

giving a discrete set of points $X_j(t), Y_j(t)$, with $j = 0, \ldots N-1$. The points X_j, Y_j, which follow the fluid flow at the interface, and thus evolve according to

$$\frac{\partial X_j}{\partial t} = u_j, \qquad\qquad\qquad \frac{\partial Y_j}{\partial t} = v_j, \qquad\qquad (B1)$$

where u_j and v_j are the velocities of the fluid interface at the point (X_j, Y_j), in the x and y directions respectively. For our numerical analysis, it is convenient to reformulate the non-dimensional equations, and work in units of length and time as $x_0 = L/\pi$ and $t_0 = [g\pi/L]^{-1/2}$ respectively. In these units the container length is π, which also facilitates a comparison with the analytical expressions. Working in these units, in terms of the Lagrangian coordinates, Eq. (4) becomes [29]

$$\frac{\partial \phi_j}{\partial t} = \frac{h}{3}\left[\frac{1}{(1 + Y_j/h)^3} - 1\right] + \frac{1}{2}\left(u_j^2 + v_j^2\right), \qquad\qquad (B2)$$

which reduces to the correpsonding gravity wave equation if one replaces the first term on the right hand side with $-Y_j$. Note the change in sign of the last term (in comparison with Eq. (4)), due to the change to the Lagrangian description. We enforce the system is periodic in j with period N, and so the Dirichlet boundary conditions at $x = 0, \pi$ are implemented by setting the values of $\{X_j, Y_j, \phi_j\}$ for $j = N/2+1, \ldots, N-1$ to be the mirror reflection of the points $j = 1, \ldots, N/2-1$ about the plane $x = \pi$. That is, we make the replacements $X_j \to 2\pi - X_j$, $Y_j \to Y_j$, and $\phi_j \to \phi_j$, and then reverse the ordering of the indices. Additionally, $u_j = 0$ for the points $j = \{0, N/2\}$, which must be constrained to lie at the walls $x = \{0, \pi\}$ throughout the evolution.

The dynamics can then be calculated as follows. Defining $Z_k = X_k + iY_k$, and the vortex strengths a_k, the potential and vortex strengths are related via the relation

$$\phi_k' = \left[\frac{1}{2} + \frac{1}{4\pi}\Im\left(\frac{Z_k''}{Z_k'}\right)\right]a_k + \frac{1}{4\pi}\sum_{\substack{j=0\\j\neq k}}^{N-1} a_j \Im\left[Z_k' \cot\left(\frac{Z_k - Z_j}{2}\right)\right] - \frac{1}{4\pi}\sum_{j=0}^{N-1} a_j \Im\left[\cot\left(\frac{Z_k - \bar{Z}_j + 2ih}{2}\right)\right] \qquad (B3)$$

where the primes denote differentiation with respect to the auxilliary variable k. Here, the second term represents the interaction between different vortices on the surface, and the third term represents the interaction with the images reflected about $y = 0$. The first term arises from regularizing the singular term $j = k$. The derivatives are evaluated using Fourier transforms, taking care to correctly zero sawtooth mode [29] (this is critical as without doing so the method is unstable). This equation gives a diagonally-dominant linear system of the form $M_{kj} a_j = \phi_k'$ that can be solved for the vortex strengths. From the vortex strengths, the velocities are then obtained from the complex velocity

$$\bar{w}_k = (u_k - iv_k) = \frac{a_k}{2Z_k'} - \frac{i}{4\pi}\left(\frac{Z_k'' a_k}{(Z_k')^2} - \frac{2a_k'}{Z_k'}\right) - \frac{i}{4\pi}\sum_{j=0j\neq k}^{N-1} a_j \cot\left(\frac{Z_k - Z_j}{2}\right) + \frac{i}{4\pi}\sum_{j=0}^{N-1}\cot\left(\frac{Z_k - \bar{Z}_j + 2ih}{2}\right). \quad (B4)$$

This completes the procedure to evolve the dynamics in time; first, given an initial surface profile Z_k and potential ϕ_k, we calculate the vortex strengths by solving the linear system Eq. (B3). We then calculate the velocities from Eq. (B4). The positions and potential are then updated according to Eqs. (B1) and (B2). Throughout we use a 4th order Runge-Kutta scheme to do the timestepping.

Standing Wave Solutions

We search for solutions that initially have zero velocity, with $\phi_j(t = 0) = 0$ and repeat themselves one period later, i.e., the surface positions and velocities satisfy $Z_j(T) = Z_j(0)$, and $\nabla\phi(x, y, 0) = \nabla\phi(x, y, T)$. If we denote $\mathcal{N}$ as a general nonlinear operator, the problem may be cast as a general nonlinear problem of the form

$$\mathcal{N}(\mathbf{v}, A_t, h) = \mathbf{0}. \qquad\qquad (B5)$$

Here h is the liquid depth, and $A_t > 0$ is the upward acceleration of the wave trough at $t = 0$. The acceleration is closely related to the wave amplitude (or steepness), however it has been shown to be a better parameterization when numerically solving for larger amplitude waves [30, 34]. Note that since the third sound waves trough-shaped, here A_t is positive, in contrast with gravity waves, which use the crest acceleration, which is negative. The two parameters h and A_t are specified to constrain the solution. The $\mathbf{v}$ specifies the vector of unknowns we need to obtain a solution; these are given by the initial surface positions X_j, and Y_j, the period T, and an auxilliary parameter α:

$$\mathbf{v} = [X_1, \ldots X_{N/2-1}, Y_0, \ldots, Y_{N/2}, T, \alpha]. \qquad\qquad (B6)$$
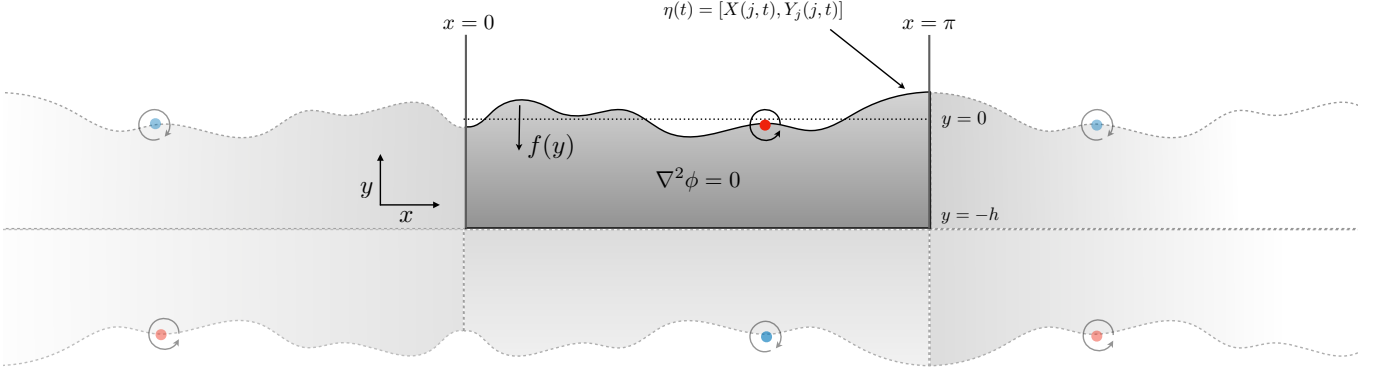
FIG. 11. Schematic showing the numerical setup of the problem. The interface between two fluids can be modelled as a distribution of singularities along the surface $\eta(t)$, i.e., a vortex sheet. Hard wall boundaries at $x = 0, \pi$ are implemented by using periodic boundary conditions on the domain $x \in [0, 2\pi]$, with reflection symmetry about $x = \pi$. The hard wall bottom at $y = -h$ is similarly incorporated by the use of image vortices.

The parameter α arises because while the velocity is periodic, the potential itself is not, being satisfied only up to a time-dependent function: $\phi_j(T) = \phi_j(0) + \text{const}$. This parameter depends on the depth of the fluid, and must introduced to maintain the mean surface depth at zero [35]. This term can also be seen in Eq. (A7), where a term $\propto t$ appears in the perturbation series solution for ϕ^1.

Eq. (B6) forms a nonlinear system of $N+2$ unknowns requiring $N+2$ equations to form a determined system. The $N+2$ constraining equations are provided by the residuals

$$\mathbf{R} = [\bar{\eta}, A_0 - A_t, \mathbf{R}^X, \mathbf{R}^Y, \mathbf{R}^\phi], \tag{B7}$$

which solve Eq. (B5) when $\mathbf{R} = \mathbf{0}$. The first constraint is the mean surface height $\bar{\eta} = \int \eta \mathrm{d}x \equiv \int \eta \frac{\mathrm{d}x}{\mathrm{d}j} dj$, which is evaluated numerically using the trapezoidal rule

$$\bar{\eta} = \frac{1}{2\pi} \sum_{k=0}^{N-1} Y_k X'_k, \tag{B8}$$

which is a spectrally accurate approximation of the integral for our choice of Fourier basis functions. The second constraint is the trough acceleration, which we evaluate using a second-order forward finite difference in time (recalling $v_0(0) = 0$):

$$A_0(0) = \frac{4v_0(\Delta t) - v_0(2\Delta t)}{2\Delta t}. \tag{B9}$$

The remaining equations defining $\mathbf{R}^X$, $\mathbf{R}^Y$, and $\mathbf{R}^\phi$ are provided by imposing appropriate symmetry conditions on the surface profile. As pointed out by Smith and Roberts [30], it is in fact not necessary to evolve for the full period T; rather one can evolve for only the quarter period $T/4$, imposing the the following symmetry conditions on the unknowns at the quarter period

$$X_j(\tfrac{T}{4}) = \left(\tfrac{2\pi}{N}j\right); \qquad\qquad j = 1, \dots, \tfrac{N}{2} - 1 \tag{B10}$$

$$Y_j(\tfrac{T}{4}) = Y_{N/2+2-j}(\tfrac{T}{4}); \qquad\qquad j = 0, \dots, \tfrac{N}{4} - 1 \tag{B11}$$

$$\phi_j(\tfrac{T}{4}) = \alpha - \phi_{N/2+2-j}(\tfrac{T}{4}); \qquad\qquad j = 0, \dots, \tfrac{N}{4} \tag{B12}$$

Eqs. (B10), (B11) and (B12) define the residuals $\mathbf{R}^X$, $\mathbf{R}^Y$ and $\mathbf{R}^\phi$ respectively. Integrating only to $T/4$ instead of T greatly improves the speed of the calculations, since each Newton-type iteration requires the equations of motion to be integrated $N+2$ times to approximate the Jacobian associated with Eqs. (B5) and (B6).

For small A_t we begin with the guess for the linearized solutions

$$X_j = j\pi/N, \qquad\qquad Y_j = a\cos(X_j), \qquad\qquad \omega_0 = \sqrt{\tanh h} \qquad\qquad \text{(B13)}$$

where $j = \{0, \ldots, N-1\}$, and $a = -A_t/\omega_0^2$ and $T = 2\pi/\omega_0$. Successive solutions are found by using the previous solution as an initial guess.

Solutions to the nonlinear problem can be found by Newton-type methods. We use Powell's dogleg-trust-region algorithm [], as implemented within MATLAB's nonlinear system solver `fsolve()`. Once a solution is found, the first-order optimality is typically less than 10^{-12}, and the sum of square residuals is typically less than 10^{-25}. Once a solution is found, we verify its accuracy by simulating for the full period T and confirming that the profile is close to the initial condition. The conserved quantities are also inspected for deviations from their initial values; similar to the mean surface height, these can be expressed as integrals over the auxilliary variable j (see e.g. Refs. [29, 30]). For the thinnest films considered, the absolute values for the quantities constrained to zero were no greater than 10^{-8}, and the relative error in the energy was no greater than 10^{-4}. For the thicker films the errors were typically several orders of magnitude smaller than this. Provided the change in acceleration is not too large between successive solutions, the dogleg algorithm typically finds a solution within 3–6 iterations.

The number of grid points N required increases with decreasing film depth h. We find accurate conservation of the conserved quantities requires $\Delta = 2\pi/N \ll 2h$. For $h = 0.025$, for example, we thus used $N = 256$. For the much thicker films, $N \sim 16 - 32$ is sufficient. If this condition is not satisfied, then the spacing between individual vortices on the surface is larger than the distance to their images reflected about $y = 0$. This leads to an innaccurate representation of the surface.

[1] G. Harris, D. McAuslan, E. Sheridan, Y. Sachkou, C. Baker, and W. Bowen, Laser cooling and control of excitations in superfluid helium, Nature Physics **12**, 788 (2016).

[2] S. Spence, Z. Koong, S. Horsley, and X. Rojas, Superfluid optomechanics with phononic nanostructures, Phys. Rev. Appl. **15**, 034090 (2021).

[3] A. Kashkanova, A. Shkarin, C. Brown, N. Flowers-Jacobs, L. Childress, S. Hoch, L. Hohmann, K. Ott, J. Reichel, and J. Harris, Superfluid brillouin optomechanics, Nature Physics **13**, 74 (2017).

[4] A. B. Shkarin, A. D. Kashkanova, C. D. Brown, S. Garcia, K. Ott, J. Reichel, and J. G. E. Harris, Quantum optomechanics in a liquid, Phys. Rev. Lett. **122**, 153601 (2019).

[5] C. G. Baker, G. I. Harris, D. L. McAuslan, Y. Sachkou, X. He, and W. P. Bowen, Theoretical framework for thin film superfluid optomechanics: towards the quantum regime, New Journal of Physics **18**, 123025 (2016).

[6] Y. L. Sfendla, C. G. Baker, G. I. Harris, L. Tian, R. A. Harrison, and W. P. Bowen, Extreme quantum nonlinearity in superfluid thin-film surface waves, npj Quantum Information **7**, 1 (2021).

[7] C. R. Bunney, S. Biermann, V. S. Barroso, A. Geelmuyden, C. Gooding, G. Ithier, X. Rojas, J. Louko, and S. Weinfurtner, Third sound detectors in accelerated motion, arXiv preprint arXiv:2302.12023 (2023).

[8] M. Aspelmeyer, T. J. Kippenberg, and F. Marquardt, Cavity optomechanics, Reviews of Modern Physics **86**, 1391 (2014).

[9] N. Brahms, T. Botter, S. Schreppler, D. W. Brooks, and D. M. Stamper-Kurn, Optical detection of the quantization of collective atomic motion, Physical Review Letters **108**, 133601 (2012).

[10] K. R. Atkins, Third and fourth sound in liquid helium ii, Phys. Rev. **113**, 962 (1959).

[11] L. A. D. Lorenzo and K. C. Schwab, Superfluid optomechanics: coupling of a superfluid to a superconducting condensate, New Journal of Physics **16**, 113020 (2014).

[12] B.-B. Li, L. Ou, Y. Lei, and Y.-C. Liu, Cavity optomechanical sensing, Nanophotonics **10**, 2799 (2021).

[13] F. Ellis and H. Luo, Third sound: Where are the solitons?, Journal of Low Temperature Physics **89**, 115 (1992).

[14] S. Nakajimia, S. Kurihara, and K. Tohdoh, Solitons in superfluid 4 he films, Journal of Low Temperature Physics **39**, 465 (1980).

[15] C. A. Condat and R. A. Guyer, Korteweg-de vries solitons and helium films, Phys. Rev. B **25**, 3117 (1982).

[16] L. Ostrovsky, E. Pelinovsky, V. Shrira, and Y. Stepanyants, Beyond the KdV: Post-explosion development, Chaos: An Interdisciplinary Journal of Nonlinear Science **25**, 097620 (2015), https://pubs.aip.org/aip/cha/article-pdf/doi/10.1063/1.4927448/13685985/097620_1_online.pdf.

[17] Y. P. Sachkou, C. G. Baker, G. I. Harris, O. R. Stockdale, S. Forstner, M. T. Reeves, X. He, D. L. McAuslan, A. S. Bradley, M. J. Davis, and W. P. Bowen, Coherent vortex dynamics in a strongly interacting superfluid on a silicon chip, Science **366**, 1480 (2019), https://www.science.org/doi/pdf/10.1126/science.aaw9229.

[18] R. Baierlein, F. Ellis, and H. Luo, Experimental determination of some nonlinear elements of third sound dynamics, Journal of low temperature physics **108**, 31 (1997).

[19] D. L. McAuslan, G. I. Harris, E. Sheridan, and W. P. Bowen, Superfluid optomechanics: Laser cooling superfluid motion, in Advanced Photonics for Communications (Optica Publishing Group, 2014) p. IM4A.1.

[20] I. Tadjbakhsh and J. B. Keller, Standing surface waves of finite amplitude, Journal of Fluid Mechanics **8**, 442–451 (1960).

[21] J. Vanden-Broeck and L. W. Schwartz, Numerical calculation of standing waves in water of arbitrary uniform depth, The Physics of Fluids **24**, 812 (1981).

[22] G. R. Verma and J. B. Keller, Three-dimensional standing surface waves of finite amplitude, The Physics of Fluids **5**, 52 (1962).

[23] D. Fultz and T. S. Murty, Experiments on the frequency of finite-amplitude axisymmetric gravity waves in a circular cylinder, Journal of Geophysical Research (1896-1977) **68**, 1457 (1963).

[24] L. R. Mack, Periodic, finite-amplitude, axisymmetric gravity waves, Journal of Geophysical Research (1896-1977) **67**, 829 (1962).

[25] W. Tsai and D. K. P. Yue, Numerical calculation of nonlinear axisymmetric standing waves in a circular basin, The Physics of Fluids **30**, 3441 (1987).

[26] V. E. Zakharov, Stability of periodic waves of finite amplitude on the surface of a deep fluid, Journal of Applied Mechanics and Technical Physics **9**, 190 (1968).

[27] J. W. Miles, On hamilton's principle for surface waves, Journal of Fluid Mechanics **83**, 153–158 (1977).

[28] P. Mason, D. Petrac, D. Elleman, T. Wang, H. Jackson, D. Collins, P. Cowgill, and J. Gatewood, Preliminary results of the spacelab 2 superfluid helium experiment, Advances in Cryogenic Engineering: Volume 31 , 869 (1986).

[29] A. Roberts, A stable and accurate numerical method to calculate the motion of a sharp interface between fluids, IMA journal of applied mathematics **31**, 13 (1983).

[30] D. H. Smith and A. J. Roberts, Branching behavior of standing waves — the signatures of resonance, Physics of Fluids **11**, 1051 (1999).

[31] T. J. Bridges, Cnoidal standing waves and the transition to the traveling hydraulic jump, The Physics of fluids **29**, 2819 (1986).

[32] P. Concus, Standing capillary-gravity waves of finite amplitude, Journal of Fluid Mechanics **14**, 568–576 (1962).

[33] C. A. Condat and R. A. Guyer, Korteweg-de vries solitons and helium films, Phys. Rev. B **25**, 3117 (1982).

[34] J. Wilkening, Breakdown of self-similarity at the crests of large-amplitude standing water waves, Phys. Rev. Lett. **107**, 184501 (2011).

[35] While α in a classical fluid is arbitrary, we remark that, in the superfluid, the interpretation of ϕ as the phase of the order parameter presumably means α could in principle be measured by interference with a phase reference.